FULL PAPER

Trace-element analysis of mineral grains in Ryugu rock fragment sections by synchrotron-based confocal X-ray fluorescence

Benjamin Bazi[1*] , Pieter Tack[1], Miles Lindner[2], Bart Vekemans[1], Ella De Pauw[1], Beverley Tkalcec[2], Frank E. Brenker[2], Jan Garrevoet[3], Gerald Falkenberg[3], Hikaru Yabuta[4], Hisayoshi Yurimoto[5], Tomoki Nakamura[6], Kana Amano[6], Megumi Matsumoto[6], Yuri Fujioka[6], Yuma Enokido[6], Daisuke Nakashima[6], Masayuki Uesugi[7], Hiroshi Naraoka[8], Takaaki Noguchi[9], Ryuji Okazaki[8], Kanako Sakamoto[10], Toru Yada[10], Masahiro Nishimura[10], Aiko Nakato[10], Akiko Miyazaki[10], Kasumi Yogata[10], Masanao Abe[10], Tatsuaki Okada[10], Tomohiro Usui[10], Makoto Yoshikawa[10], Takanao Saiki[10], Satoshi Tanaka[10], Fuyuto Terui[11], Satoru Nakazawa[10], Shogo Tachibana[12], Sei-ichiro Watanabe[13], Yuichi Tsuda[10] and Laszlo Vincze[1]

Abstract

A fundamental parameter-based quantification scheme for confocal XRF was applied to sub-micron synchrotron radiation X-ray fluorescence (SR-XRF) data obtained at the beamline P06 of the Deutsches Elektronen-Synchrotron (DESY, Hamburg, Germany) from two sections C0033-01 and C0033-04 that were wet cut from rock fragment C0033 collected from Cb-type asteroid (162173) Ryugu by JAXA's Hayabusa2 mission. Trace-element quantifications show that C0033 bulk matrix is CI-like, whereas individual mineral grains (i.e., magnetite, pyrrhotite, dolomite, apatite and breunnerite) show, depending on the respective phase, minor to strong deviations. The non-destructive nature of SR-XRF coupled with a new PyMca (a Python toolkit for XRF data analysis)-based quantification approach, performed in parallel with the synchrotron experiments, proves to be an attractive tool for the initial analysis of samples from return missions, such as Hayabusa2 and OSIRIS-REx, the latter returning material from a B-type asteroid (101955) Bennu in 2023.

Keywords: X-ray fluorescence, Confocal, Quantification, Fundamental parameter method, Ryugu, Hayabusa2

---

*Correspondence: benjamin.bazi@ugent.be

[1] Department of Chemistry, Ghent University, Krijgslaan 281 S12, B-9000 Ghent, Belgium
Full list of author information is available at the end of the article

Bazi *et al. Earth, Planets and Space*   (2022) 74:161

Page 2 of 17

Graphical Abstract
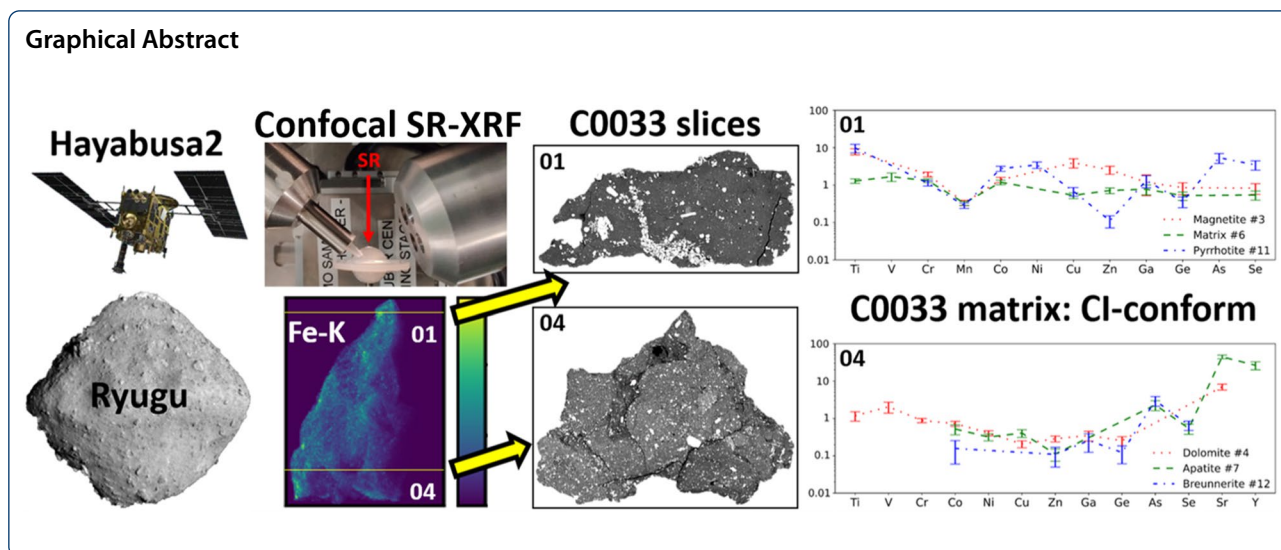
Introduction

We will discuss the quantification results obtained from pristine material returned to Earth by Japan Aerospace Exploration Agency's (JAXA) Hayabusa2 mission from Cb-type asteroid (162173) Ryugu on December 6, 2020. The investigated mm-sized rock fragment C0033 was collected into sample Chamber C during the second touchdown (TD2) on Ryugu's surface on July 11, 2019 from the C01-Cb area of Ryugu, about 20 m away from the artificial crater created earlier by the small carry-on impactor (SCI). It is assumed that sample Chamber C (total mass ∼ 2 g) contains both surface and sub-surface material exposed by the 2 kg copper SCI (Saiki et al., 2017, 2021; Arakawa et al., 2020; Tachibana et al., 2022), receiving its kinetic driving force from a polymer-bonded explosive (Ito et al., 2021).

The Hayabusa2 mission objective was to investigate formation, evolution and volatile content of a pristine carbonaceous asteroid (Watanabe et al., 2019). The Cb-type carbonaceous asteroid Ryugu was expected to be related to carbonaceous chondrites of CI or CM-type (Sugita et al., 2019) which are a prime source to study early Solar System processes. For this purpose, however, pristine material directly collected from an asteroid's surface is particularly useful, to avoid the risks of any terrestrial contamination of water and organic matter (e.g., Tachibana, 2021), and any heating and stress potentially suffered during atmospheric entry. Such heating effects have been observed, for example, in the case of micrometeorites (Greshake et al., 1994; Rudraswami et al., 2015) and the formation of ferrihydrate and sulfate minerals, for example, have been observed in CI chondrites due to terrestrial weathering, (Gounelle and Zolensky, 2001).

Another ongoing asteroid mission is NASA's OSIRIS-REx sample return mission to B-type asteroid (101955)

Bennu, currently returning regolith samples to Earth (Lauretta et al., 2019).

Synchrotron radiation X-ray fluorescence (SR-XRF) spectroscopy has been used as a non-destructive analytical tool to image and quantify elemental abundances in cometary (Flynn et al., 2006; Zolensky et al., 2006; Flynn, 2007; Schmitz et al., 2009; Silversmit et al., 2009) and interstellar (Westphal et al., 2014; Brenker et al., 2014) material from previous sample return missions. In this article, results from a confocal fundamental parameter-based SR-XRF quantification scheme are presented, based on an approach originally developed to obtain quantitative trace-element information from return samples originating from comet Wild2 (Schoonjans et al., 2012).

Experimental

Trace-element concentrations of individual minerals, i.e., apatite, dolomite, breunnerite, (framboidal) magnetite and pyrrhotite, in the studied C0033 sections were derived from SR-XRF spectra obtained at the PETRA III facility of the Deutsches Elektronen-Synchrotron (DESY) in Hamburg, Germany, with the energy-dispersive micro-XRF setup (Fig. 1) at the Hard X-ray Micro/Nano-Probe beamline P06 (Schroer et al., 2010). The experiment made use of a sub-micron beam of X-rays monochromatized by a Si(111) double-crystal monochromator and subsequently focused by a Kirkpatrick-Baez (KB) mirror pair. Confocal data sets were acquired using an XOS focusing optic (Fig. 1) with a focal distance of 2.2 mm and an enclosure length of 27.5 mm, coupled with a Vortex-EM silicon drift detector (SDD) (model No: 578-VTX-EM-300). This polycapillary optic consists

Bazi *et al. Earth, Planets and Space* (2022) 74:161

Page 3 of 17
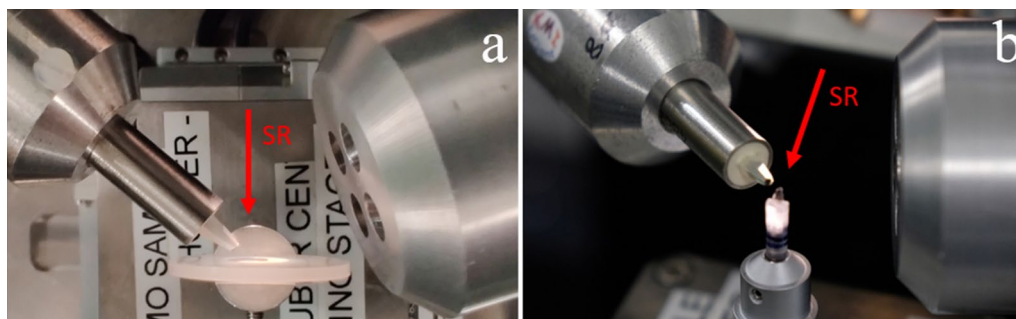
Fig. 1 XRF detection setup used at beamline P06 to analyse **a** Ryugu sections C0033-01 and C0033-04 fixed in epoxy disks and **b** the geological glass reference material ATHO-G. Confocal SDD detector on the left, 4-element SDD detector on the right. Both are positioned, respectively, under opposite angles of 47° and 72°. The incident SR beam is indicated with a red arrow

of an array of many glass fibres with micron-sized internal channels, oriented to only accept X-ray photons originating from a micron-sized volume. Polycapillaries guide the X-rays based on repeated total reflections inside the glass channels when the X-rays hit a surface with a lower angle than the critical angle of total reflection $\theta_C(mrad) \approx 30/E(keV)$, where E is the X-ray photon energy. For a more detailed explanation of detecting fluorescent X-rays of a selected area with a polycapillary optic, the reader is referred to Vincze et al. (2004). The single-element SDD has a 50 mm^2 active area collimated on chip, having a 350 μm crystal thickness, and a 12 μm Be window combined with an Xspress 3 readout system by Quantum Detectors Limited. After confocal alignment with a 10 mμ GoodFellow stainless steel wire, the detector optic showed a FWHM acceptance of 16.4 μm at Fe-K$_\alpha$, defining the maximum probed dimension within the sample along the X-ray beam at 6.4 keV energy. The confocal depth resolution at different energies E can be approximated by $16.4\mu m * 6.4keV/E(keV)$ (Vincze et al., 2004). Imaging data sets were acquired using a 4-element Vortex-ME4 SDD (model No: 865-VTX-ME4-300) with a total collimated active area of 170 mm^2, a 350 μm crystal, a 12.5 μm Be window and an Xspress 3 Mini readout system. The latter used an Al collimator to minimize the spectral contribution of background scatter and undesired signals from the sample environment. For the SR-XRF measurements, the samples were probed in a position characterised by a 240 nm (H) × 200 nm (V) beam size at an excitation energy of 20.5 keV. As the Ryugu material was found to be rich in Fe, the incident flux was attenuated accordingly to minimize detector pile-up. For confocal point measurements, the beam was 90% attenuated. For overview scans and point measurements with the 4-element detector, the beam was attenuated by 90% and 99%, respectively. Although most of the

flux had to be attenuated, the P06 beamline was chosen for its small beamsize, which was needed to investigate the micron-sized mineral grains. In the experimental setup, the incident X-ray beam impinged on the sample at an angle of 90° and the confocal and multi-element detectors were positioned, respectively, under opposite scatter angles of 47° and 72° with respect to the primary beam, as shown in Fig. 1.

Materials and methods
Sample description
Two polished Ryugu sections C0033-01 and C0033-04, had been wet cut using a diamond wire saw (130 mμ diameter) and ethanol from rock fragment C0033 and mounted in epoxy resin (Nakamura et al., 2022). C0033 was characterised by a size of 1.99 mm × 1.33 mm × 0.92 mm, a mass of 1.99 mg and an average bulk density of 1.92 g/cm^3 (Nakamura et al., 2022). The size and density of sample C0033 were estimated based on synchrotron radiation computed tomography (SR-CT) data obtained at beamline BL20XU of the Super Photon Ring (SPring-8) Hyōgo Prefecture, Japan (Nakamura et al., 2022). Both sections, with a thickness of ∼ 200 μm, had been hand-polished using ethanol, C0033-04 was additionally polished under dry conditions and carbon-coated to study the effect of possible ethanol absorption by the Ryugu matrix (Nakamura et al., 2022). A 93 μm, rhyolitic glass, geological MPI-DING reference material, ATHO-G (Fig. 1b), was used for the presented quantitative procedure with certified reference concentrations given by Borisova et al. (2010). The two polished sections were investigated using a scanning electron microscope (SEM), including SEM-based energy-dispersive X-ray spectroscopy; (SEM–EDX) and SR-XRF spectroscopy.

Imaging and main-element quantification

For the identification and localization of mineral grains in these sections, backscattered electron (BSE) images with pixel sizes of 80 nm were obtained with a JEOL JSM 6490 electron microscope utilizing an acceleration voltage of 15 kV. With this instrument, the probe current is controlled by the dimensionless "spot size" setting, and the latter was set at 60 during the SEM data acquisition. An intensity calibration on a cobalt reference was performed prior to the measurements. The main-element composition of these mineral grains were acquired with SEM–EDX spectroscopy following the "remote standards" protocol (Newbury et al., 2013). These concentrations were thus obtained by comparing the recorded intensities with a library of standard reference intensities derived from pure elements and stoichiometric compounds, the oxygen concentration (not for pyrrhotite) was calculated by stoichiometry, and the results were normalised to 100 wt%. Considering the relative errors for "remote standards" analysis fall in the range $\pm 25\%$ (Newbury et al., 1995), the trace-element quantification scheme is tested for this error range and discussed further in "Experimental and interpolated MC-based yields" section. The BSE images together with superimposed SR-XRF overview scans allowed for individual confocal point analysis providing trace-element information. Although the BSE images had better pixel resolution than the SR-XRF images, both image data sets could be compared as most mineral grains were micron-sized. For image overlays, BSE and SR-XRF overview scans were imported into the commercial software Affinity Designer. Images were scaled (preserving the aspect ratio) onto the same size on the computer screen, according to their magnification and overlain by hand. The orientation (translation and rotation) of the overlay was then achieved using distinct features, unambiguously recognizable in both images, such as distinct mineral grains (e.g., magnetite or apatite grains, recognizable in the BSE image and by their Fe, or Ca signal, respectively). As the penetration depth varies between X-rays (tens of μm for the used experimental parameters) and electrons (a few μm at most) as a source, sub-surface mineral grains were also detectable with SR-XRF which are otherwise missed by BSE and SEM–EDX spectroscopy.

Confocal sub-micron SR-XRF quantification

Each SR-XRF point measurement was preceded by a small overview scan performed around the point of interest, defined by SEM work, to establish its exact position in the beam. Confocal depth scans were performed to check the mineral grain's depth below the surface and to match the confocal volume. The individual mineral grain size was estimated based on SR-CT data obtained at beamline BL20XU of SPring-8 (Nakamura et al., 2022). The software Drishti (Limaye, 2012) was used for the visualization and orientation of CT data with a spatial resolution of 3.36 μm/voxel. The latter was obtained after image pixel binning of the original CT data by a factor of 4 (CT image areas of 4×4 pixels are averaged to 1 pixel), to reduce the amount of total data, speeding up data transfer between several research groups during the Initial Analysis phase. As most of the analysed mineral grains proved to be smaller than the polycapillary depth acceptance, a matrix correction was performed using elemental net-peak intensities based on a $\rho \cdot T$ correction, and is presented as Eq. 1. This specific matrix correction approximation can be applied in the understanding that all analysed mineral grains were located on the surface and always had a density greater than the matrix.

$$I_{i,K_\alpha}^{grain} = I_{i,K_\alpha}^{grain+matrix} - I_{i,K_\alpha}^{matrix} * \frac{\rho^{matrix}}{\rho^{grain}} * \left(1 - \frac{T^{grain}}{FWHM_{acc}}\right) \tag{1}$$

with I_{i,K_α}^{grain}, $I_{i,K_\alpha}^{grain+matrix}$ and I_{i,K_α}^{matrix} the net-peak K_α line intensity of element i from only the grain, from both the grain and the matrix, and from only the matrix, respectively, ρ^{matrix} the density of the matrix, ρ^{grain} the density of the grain, T^{grain} the size of the grain and $FWHM_{acc}$ the sample depth acceptance by the polycapillary which is inversely proportional with the energy of the fluorescence photons.

The spectra corresponding to confocal SR-XRF point measurements were normalised for primary beam flux and detector dead time. Further data handling follows the confocal SR-XRF quantification model as presented by Schoonjans et al. (2012). Net-peak intensities of the K_α fluorescent lines were obtained using the PyMca5 software package (Solé et al., 2007). The experimental elemental yields for element i and the sample absorption correction coefficient are defined as Eqs. 2 and 3, respectively:

$$Y_{i,exp} = \frac{I_{i,K_\alpha}^{(s)}}{I_0^{(s)} w_i^{(s)} A_{i,corr}^{(s)} \rho^{(s)} T^{(s)} t^{(s)}} \tag{2}$$

$$A_{i,corr} = \frac{1}{\rho T} \sum_{j=1}^{N} \left[\prod abs_{\Delta x_j}^0 \cdot fluo_{\Delta x_j} \cdot \prod abs_{\Delta x_j}^1 \cdot scale_{\Delta x_j} \right] \tag{3}$$

with I_{i,K_α} the net-peak K_α line intensity of element i, I_0 the primary beam flux, w_i the weight fraction of element i, ρ the density, T the thickness, t the detector live time and (s) refers to the standard reference material. The layer of interest within the sample along the incident beam path

'x', in this case the approximately 200 μm sections, is partitioned in a large number of narrow intervals Δx_j. It was chosen to evaluate the sample absorption every 0.5 μm, leading to a total number of intervals 'N' of approximately 400. Decreasing Δx_j further gives no significantly different results and only increases the total calculation time. $\prod abs_{\Delta x_j}^0$ is the absorption from an air layer of $\sim$ 25 cm (i.e., air path between the sample and the exit window of the KB mirror pair) before the layer of interest at the primary energy and from the intervals within the layer of interest along the incident beam, $fluo_{\Delta x_j}$ is the generated fluorescence intensity in Δx_j, whereas $\prod abs_{\Delta x_j}^1$ is the attenuation from the layer of interest and from an air layer of $\sim$ 6 cm (i.e., combination of the polycapillary focal distance, its length, and additional distance till the detector chip) for the fluorescence, and $scale_{\Delta x_j}$ the contribution of interval Δx_j to the spectral line recorded by the detector. As the beam size is much smaller than the polycapillary acceptance, a 1D model of the confocal detection was used.

Based on the experimental yield values, a weighted linear least squares polynomial fit was applied to produce interpolated yield values $Y_{i,fit}$ for the elements present in the reference material as well as for some that are absent. Concentration values for the unknown samples (u) are then calculated with Eq. 5 in an iterative manner. After each iteration the concentration values are used to update the total mass attenuation cross sections $\mu_{\rho,total}$ (Eq. 4) which redefine $A_{i,corr}$.

$$\mu_{\rho,total} = \sum w_i * \mu_{\rho,i}(E) \tag{4}$$

The element specific mass attenuation cross sections $\mu_{\rho,i}$ were obtained with the xraylib library for X-ray–matter interactions (Schoonjans et al., 2011a, 2011b). The iterative calculation of concentrations was stopped in case convergence was reached, i.e., when the difference in subsequent iteration values was smaller than 1%. For the initial absorption correction, the main sample composition elemental concentration values, derived from SEM–EDX measurements, were used. SEM–EDX data were also used as starting sample composition for the analysed mineral grains in most cases. For magnetite measurements, stoichiometric Fe and O concentrations were used. These initial values were kept fixed during the iterative process. The latter allowed to drastically speed up the time needed to reach convergence, typically only few iterations (≤ 3) were needed, as $\mu_{\rho,total}$ is largely dictated by the main elements:

$$w_i^{(u)} = \frac{I_{i,K_\alpha}^{(u)}}{I_0^{(u)} Y_{i,fit} A_{i,corr}^{(u)} \rho^{(u)} T^{(u)} t^{(u)}} \tag{5}$$

A brute-force Monte Carlo (MC) approach was used for error estimation based on variance analysis of the calculated results. Based on a high-quality pseudorandom number generator PCG64 (O'Neill, 2014), the relevant quantification parameter values are varied around their original mean and their influence is estimated on the final results. Distance (i.e., depth of the confocal volume parallel to the incident beam and parallel to the detector) and density values were both varied using a uniform distribution. The distance values are assumed to have a 10% error (larger deviations would be visible in the confocal depth scans), the density values of the analysed mineral grains together with their error ranges were taken from Chang et al., 1996 and Bowles et al., 2011. The density of the matrix itself was taken as the average bulk density (Nakamura et al., 2022) but with an error of 10% to take into account the presence of higher density mineral grains, pores and fractures. For each individual parent spectrum (reference and mineral grains) 50,000 Poisson varied spectra were generated and fitted with PyMca, giving a distribution of elemental net-peak intensities as a function of random contributions by the relevant experimental parameters. Based on this, 50,000 sets of experimental and interpolated yields were produced, after which 50,000 sets of concentration values were calculated by randomly taking a set of interpolated yields and a set of net-peak intensities, providing a distribution of the results. This amount of calculations proved sufficient for the error estimation process, increasing the latter to 100,000 did not give any significant change to the calculated concentration values and would only increase the overall calculation time. Charts visualizing the Monte Carlo uncertainty estimation methods for the calculation of the elemental yields and mineral grain weight fractions are presented as Additional file 1 and Additional file 2, respectively.

Results and discussion

Section C0033-01 is dominated by a prominent magnetite rich vein that cross-cuts the complete section (Fig. 2a). A high-resolution SR-XRF scan of the vein area displayed as an RGB (Ca–Fe–S) image (Fig. 2b) confirms that the vein is largely composed of magnetite (green) grains but also includes some rare pyrrhotite (blue–green) grains and laths. Also present within the vein are several Ca-rich grains 5–10 μm in size.

Section C0033-04 is a cross-sectional slice of a Ca-rich part of rock fragment C0033 (Fig. 3) and shows a widespread abundance of magnetite grains and framboids, pyrrhotite laths and fragments, and a light grey matrix in which darker areas of less dense material can be observed. Four areas (Fig. 3, yellow boxes) were selected
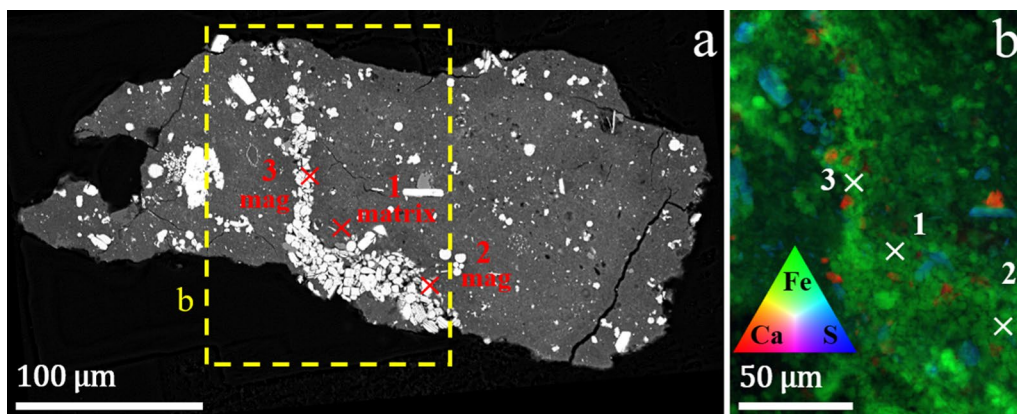
Fig. 2 **a** BSE image of C0033-01 after epoxy fixation. The magnetite vein is highlighted in yellow. **b** High-resolution SR-XRF overview scan (200 nm step size) of the magnetite region presented in **a**. Unlike the BSE image that includes only surface information, the SR-XRF image includes additional SR-XRF signals received from subsurface layers of C0033-01, which extends to a broader area beneath the surface. The SR-XRF overview scan is displayed as an RGB image showing the K-line intensities of Ca (Red), Fe (Green), and S (Blue). Confocal point analyses #1, #2 and #3 are indicated with a cross
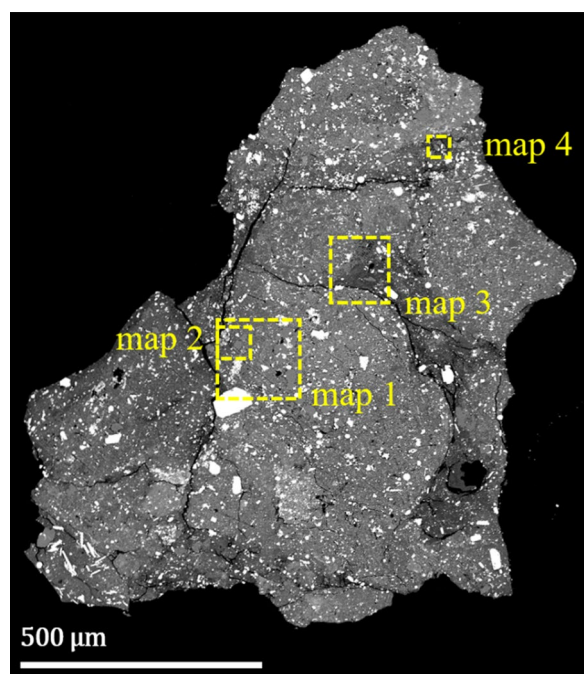
Fig. 3 BSE image of C0033-04 after epoxy fixation. SR-XRF overview scans are highlighted in yellow

for the performance of high-resolution SR-XRF scans (maps 1, 2, 3 and 4). The high-resolution SR-XRF scans (Fig. 4b, d, f and g) reveal the distribution of Ca-rich phases (such as apatite and dolomite) and Fe-rich phases (such as magnetite and pyrrhotite).
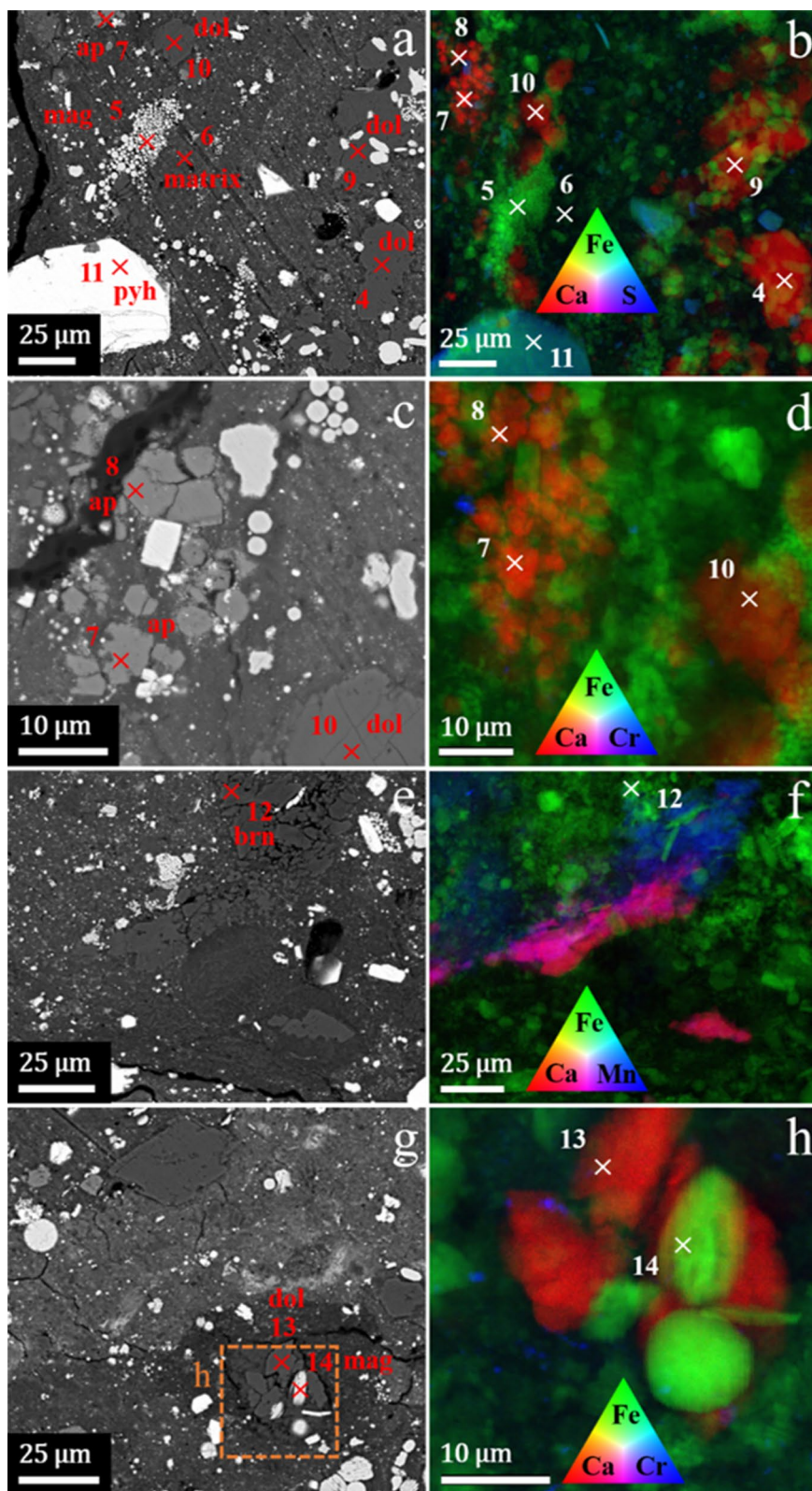
In the following results that were acquired using the confocal fundamental parameter method-based quantification are discussed.
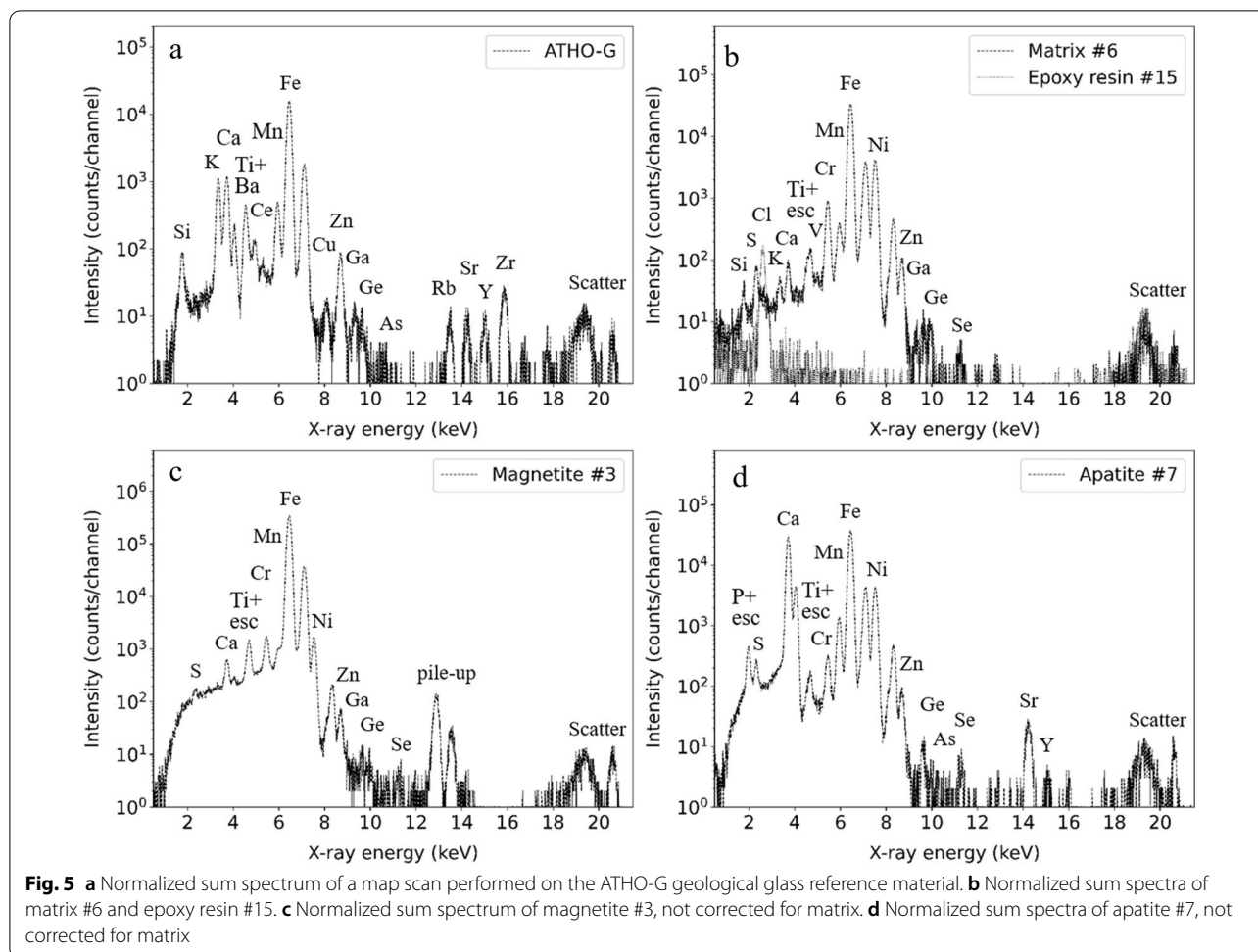
Experimental and interpolated MC-based yields

Detection limit (DL) and elemental yield calculations were based on the MPI-DING geological glass standard ATHO-G (Borisova et al, 2010) as it is well-documented and was also chosen for the confocal trace-element quantification of NASA's STARDUST interstellar dust particles (Schoonjans et al., 2012; Brenker et al., 2014) due to minimal overlap between the observed K_α peaks. A 2D scan (to reduce local inhomogeneity) of 11×11 points with a stepsize of 1 µm was performed with t = 10 s live time, the resulting normalized sum spectrum is presented in Fig. 5a. The longitudinal position of the standard, which was perpendicular to the incident X-ray beam, along the source-sample axis was optimized via depth scans for total count rate. The resulting primary

(See figure on next page.)
Fig. 4 BSE images (**a**, **c**, **e**, **g**) of maps 1, 2, 3 and 4, respectively (indicated in Fig. 3). High-resolution non-confocal SR-XRF scans displayed as RGB images showing the K-line intensities of Ca (R), Fe (G), and S (B) (b, 250 nm step size), Ca (R), Fe (G), and Cr (B) (d and h, 100 nm step size) and Ca (R), Fe (G), and Mn (B) (f, 200 nm step size). Red/white crosses mark the points, where confocal point analyses were performed, the results of which are shown in Tables 2 and 3. Due to difficult sample positioning, there is a slight misalignment between the BSE and SR-XRF images

Bazi *et al. Earth, Planets and Space*   (2022) 74:161

Page 7 of 17

Fig. 4 (See legend on previous page.)

Bazi *et al. Earth, Planets and Space* (2022) 74:161

Page 8 of 17

Fig. 5 **a** Normalized sum spectrum of a map scan performed on the ATHO-G geological glass reference material. **b** Normalized sum spectra of matrix #6 and epoxy resin #15. **c** Normalized sum spectrum of magnetite #3, not corrected for matrix. **d** Normalized sum spectra of apatite #7, not corrected for matrix
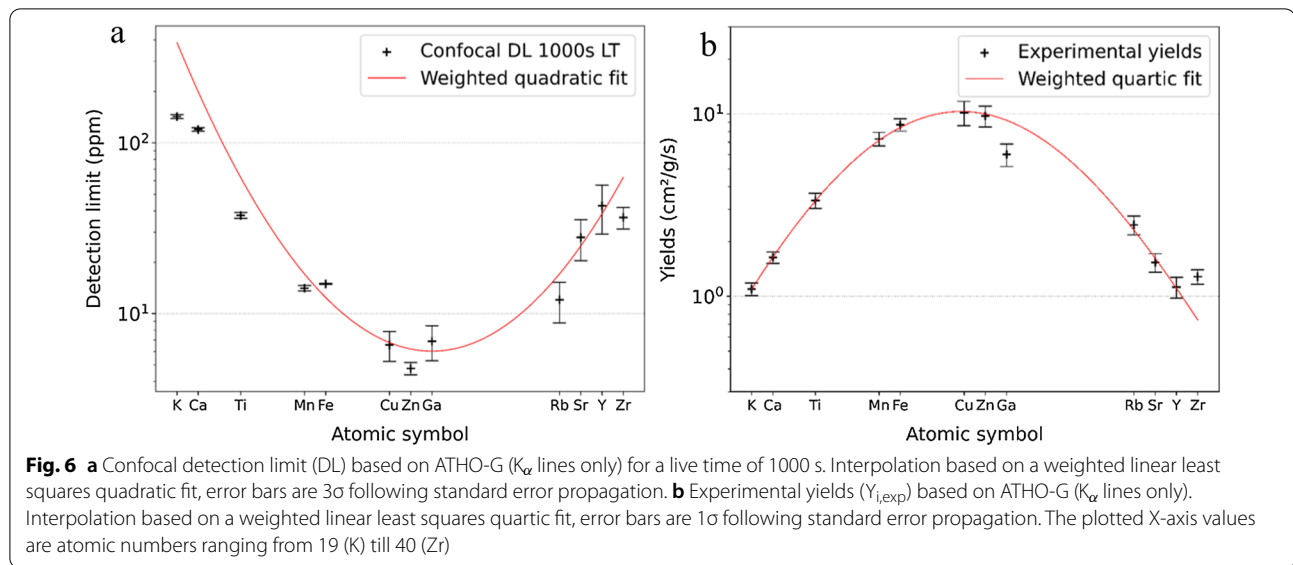
excitation depth and confocal volume depth, which are explained by Schoonjans et al. (2012), were 27 μm and 39.6 μm, respectively. The normalized sum spectra of Ryugu point measurements of magnetite #3, matrix #6, apatite #7 and epoxy resin #15 are presented in Fig. 5b–d. The magnetite #3 spectrum comes from "Introduction" section (Fig. 2), the other spectra come from "Results and discussion" section (Fig. 4). The epoxy resin was measured as a blank and did not show any impurities, except for chlorine which is not included in the list of available elemental yields.

The confocal DL (Beckhoff et al., 2007) derived from the K_α fluorescent peaks measured from the ATHO-G standard is presented in Fig. 6a, scaled to the $t = 1000$ s live time used for all mineral grain point measurements. Error bars are 3 σ, following standard error propagation, and were used to calculate a weighted linear least squares polynomial fit, an order of 2 gave the best result. The fit

does slightly overestimate the DLs of the lower Z elements (Z < Mn) but this does not affect the final quantification results as the DLs are only used reliably to check the presence of elements in samples within an order of magnitude. To check the reliability of the final quantified results, these were tested against the interpolated DL values, e.g., elements with small calculated concentration values, which are comparable to their detection limit, should have small peaks above the background. If not the case, some density and/or thickness values still deviated from their optimal values.

The experimental yield values based on the K_α fluorescent peaks of ATHO-G are presented in Fig. 6b and Table 1. Error bars are 1 σ, following standard error propagation, and were used to calculate a weighted linear least squares polynomial fit, an order of 4 gave the best result. Ga and Zr were not included in the fit as their net-peak intensities did not follow the trend established by the
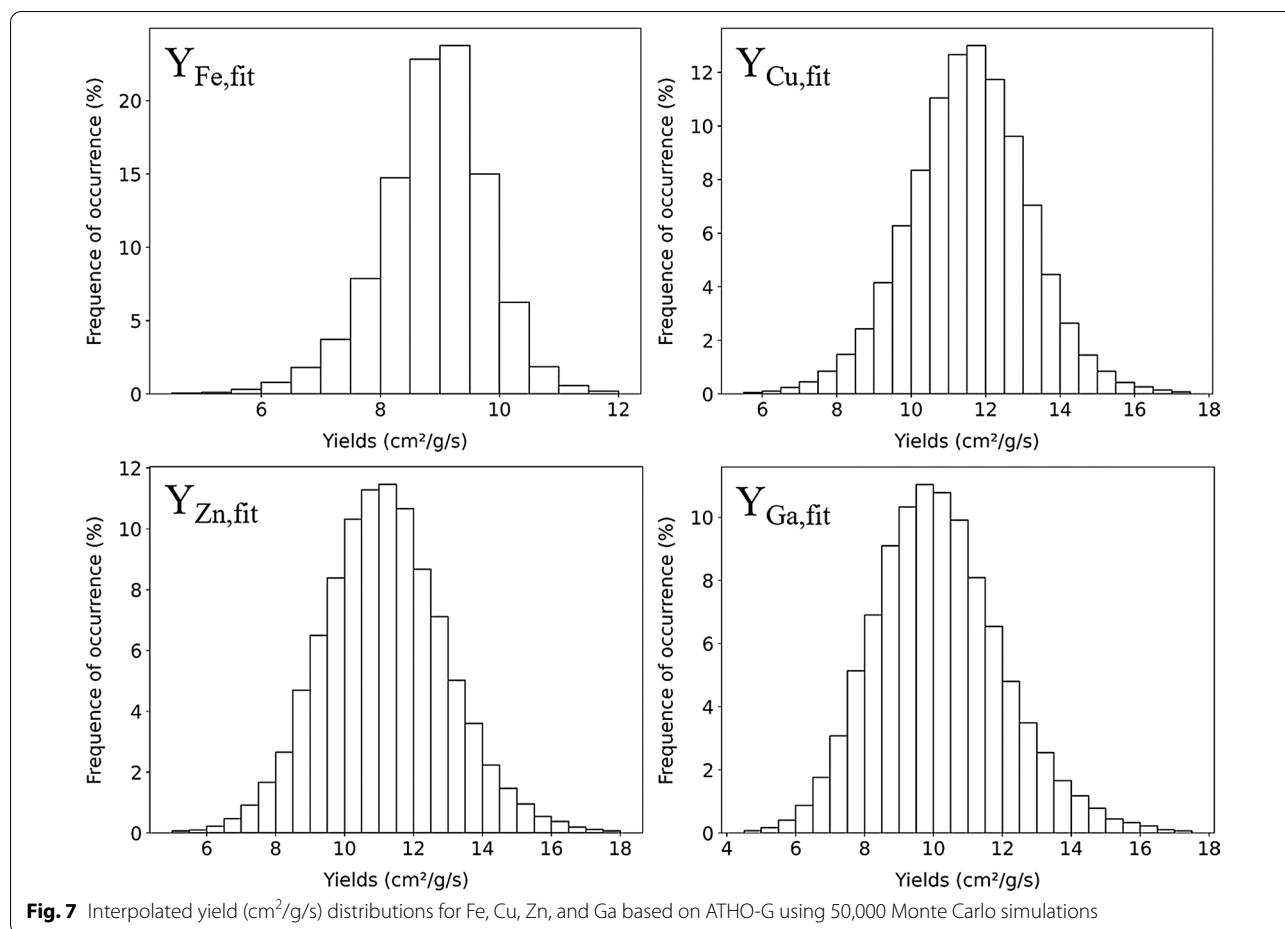
Fig. 6 **a** Confocal detection limit (DL) based on ATHO-G (K_α lines only) for a live time of 1000 s. Interpolation based on a weighted linear least squares quadratic fit, error bars are 3σ following standard error propagation. **b** Experimental yields ($Y_{i,exp}$) based on ATHO-G (K_α lines only). Interpolation based on a weighted linear least squares quartic fit, error bars are 1σ following standard error propagation. The plotted X-axis values are atomic numbers ranging from 19 (K) till 40 (Zr)

Table 1 Experimental and interpolated Monte Carlo-based yields ($cm^2/g/s$) of ATHO-G reference

	Experimental yields		Interpolated MC-based yields	
	Elemental yield	Standard deviation	Elemental yield	Standard deviation
K	1.094	0.086	1.138	0.055
Ca	1.634	0.12	1.574	0.066
Ti	3.346	0.319	3.086	0.187
V	/	/	4.244	0.315
Cr	/	/	5.667	0.486
Mn	7.289	0.625	7.272	0.688
Fe	8.712	0.671	8.891	0.909
Co	/	/	10.295	1.143
Ni	/	/	11.243	1.389
Cu	10.161	1.551	11.555	1.631
Zn	9.732	1.266	11.172	1.825
Ga	5.992	0.841	10.174	1.908
Ge	/	/	8.753	1.837
As	/	/	7.144	1.613
Se	/	/	5.565	1.280
Rb	2.463	0.289	2.193	0.287
Sr	1.536	0.178	1.593	0.146
Y	1.122	0.147	1.202	0.208
Zr	1.281	0.117	0.928	0.174

majority of elemental yields, being either underestimated or overestimated, respectively. The deviation between the interpolated yield curve and the experimental elemental yields can indicate increased uncertainties for Ga and Zr

in terms of quantitative results. Si is not included as its experimental yield calculation was not reliable; therefore, it was not possible to reliably interpolate the experimental yield values between Si and K. The interpolated MC-based yields (50,000 simulations) are presented in Table 1. The corresponding elemental yield distribution histograms for Fe, Cu, Zn and Ga are presented in Fig. 7. The shape of these curves is primarily Gaussian-like which can be explained by the large number of independent (random) variables influencing the calculated concentration values, hence approaching Gaussian distribution as a result of the central limit theorem (CLT). The distribution is also influenced by the Poisson distribution used for the perturbation of the ATHO-G spectral line intensities during the variance analysis.

The concentration values and standard deviations (resulting from 50,000 trials in the variance analysis) calculated from the Ryugu point analyses (Figs. 3, 4) for the matrix (points #1 and #6), magnetite (points #2, #3, #5 and #14) and pyrrhotite (point #11) are presented in Table 2, and for the dolomite (points #4, #9, #10 and #13), apatite (points #7 and #8) and breunnerite (point #12) in Table 3. 'nd' means 'not detected' which notes the fact that the element was either not present or present below DL. "Others" denotes the combined weight fraction of all major/minor elements whose concentration values could not be determined accurately by SEM–EDX or SR-XRF analysis. For all confocal point measurements this mostly consists of oxygen (O), for the matrix points this is extended with the elements below Si ($Z < 14$). To iteratively update $\mu_{\rho,total}$ in the quantification method, the

Fig. 7 Interpolated yield (cm²/g/s) distributions for Fe, Cu, Zn, and Ga based on ATHO-G using 50,000 Monte Carlo simulations

leftover unknown weight percent of the analysed point to reach 100 wt% (the "others" weight percent) has to be assigned to a single element to be able to calculate a mass attenuation cross sections, see Eq. 4. For this, oxygen (O) was used as the "others" representative as the majority of the analysed mineral grains contain O as a major element. Main elements were not quantified again with the SR-XRF technique as SEM–EDX is considered more reliable for low-Z elements, and the iterative process would have otherwise required an increase in total processing time by a factor 3–4. The trace-element concentration values for mineral grains apatite #8, dolomite #10 and magnetite #14 are less accurate due to interference with nearby non-matrix regions. Apatite #8 is a grain protruding above a fracture (visible on Fig. 4c) leading to a too strong matrix correction, dolomite #10 has an Fe-rich region in proximity below the grain (visible with a confocal depth scan) and magnetite #14 has slight dolomite interference below it (visible on Fig. 4h).

The weight fraction distribution histograms for Co, Cu, Zn and Y for apatite #7 of Ryugu section C0033-04 are presented in Fig. 8. The shape of these curves is mainly Gaussian due to CLT but not entirely, the minor visible Poisson shape is related to the variance analysis of the parent apatite spectrum. The smooth profiles of these distributions also indicate that all the independent (random) variables were sampled sufficiently in the 50,000 MC simulations, providing a reliable error estimation.

The CI normalised (Lodders, 2010) concentration values and standard deviations of trace elements in magnetite #3, matrix #6 and pyrrhotite #11 are presented in Fig. 9a. The trace element concentrations for the matrix reveal a flat pattern in close conformity to the CI bulk values (Lodders, 2010) supporting a classification of Ryugu material as CI-like (Nakamura et al., 2022; Yokoyama et al., 2022). The pyrrhotite grain #11 (and partly also the magnetite grain #3) reveals more variance and fluctuations. In particular, the pyrrhotite

Bazi *et al. Earth, Planets and Space*   (2022) 74:161

Page 11 of 17

Table 2 Concentrations with standard deviations obtained for matrix, magnetite (mag) and pyrrhotite (pyh)

	#1	#6	#2	#3	#5	#14	#11
	Matrix	Matrix	Magnetite	Magnetite	Magnetite	Magnetite	Pyrrhotite
ρ(g/cm^3)	1.73–2.11	1.73–2.11	5.2	5.2	5.2	5.2	4.58–4.79
T^{grain}(μm)	/	/	14–17	14–17	14–17	10–14	27–30
Si	10.7†	10.7†	nd	nd	nd	nd	nd
S	5.35†	5.35†	nd	nd	nd	nd	41.33$^{\ast}\pm$0.39*
Ca	0.922†	0.922†	nd	nd	nd	nd	nd
Ti	0.10$^*\pm$0.01*	0.06$^*\pm$0.01*	0.37$^*\pm$0.07*	0.36$^*\pm$0.07*	0.36$^*\pm$0.08*	0.23$^*\pm$0.06*	0.44$^*\pm$0.11*
V	35$\pm$25	91$\pm$23	76$\pm$63	nd	nd	nd	nd
Cr	0.21$^*\pm$0.02*	0.35$^*\pm$0.04*	0.13$^*\pm$0.04*	0.51$^*\pm$0.07*	0.07$^*\pm$0.03*	nd	0.30$^*\pm$0.05*
Mn	457$\pm$57	630$\pm$76	202$\pm$59	649$\pm$102	672$\pm$111	2.35$^*\pm$0.38*	547$\pm$92
Fe	18.5†	18.5†	72.36	72.36	72.36	72.36	53.98$^{\ast}\pm$0.51*
Co	0.18$^*\pm$0.03*	0.06$^*\pm$0.01*	328$\pm$68	698$\pm$109	655$\pm$106	163$\pm$95	0.14$^*\pm$0.02*
Ni	1.08†	1.08†	nd	nd	nd	nd	3.73$^{\ast}\pm$0.75*
Cu	41$\pm$8	69$\pm$12	391$\pm$117	516$\pm$143	443$\pm$136	nd	89$\pm$24
Zn	69$\pm$12	231$\pm$40	669$\pm$169	820$\pm$199	726$\pm$188	619$\pm$291	36$\pm$13
Ga	4$\pm$1	8$\pm$2	20$\pm$7	12$\pm$7	23$\pm$10	27$\pm$11	13$\pm$5
Ge	8$\pm$2	17$\pm$4	34$\pm$10	28$\pm$10	32$\pm$11	55$\pm$18	12$\pm$4
As	nd	nd	nd	nd	16$\pm$5	nd	9$\pm$3
Se	12$\pm$3	11$\pm$3	14$\pm$5	17$\pm$5	20$\pm$6	13$\pm$4	70$\pm$20
Sr	nd	nd	nd	nd	nd	nd	nd
Y	nd	nd	nd	nd	nd	nd	nd
Others	62.90$^*\pm$0.06*	62.87$^*\pm$1.38*	26.97$^*\pm$0.13*	26.50$^*\pm$0.18*	26.95$^*\pm$0.14*	24.97$^*\pm$0.41*	0$^*\pm$0*

For the Fe concentration in magnetite it was preferred to use its stoichiometric value as the SEM–EDX quantification of O is less reliable. Data in ppm, except for the asterisk (*) representing data in wt%, the double asterisk (⁎) representing SEM–EDX data in wt% and the dagger (†) representing CI chondrite composition data from Lodders, 2010 in wt%. nd = not detected

(#11) grain displays an approximate five-to-tenfold enrichment in Co, Ni and Se and an approximate tenfold depletion in Zn, relative to bulk CI values, which resembles the concentrations recorded by SR-XRF for pyrrhotite found in chondrules within the CM chondrite QUE 97990 (Singerling et al. 2021). However, within the error margins, the results for pyrrhotite are also roughly in agreement with the trace element concentrations recorded in pyrrhotite grains in Orgueil CI chondrite (Greshake et al. 1997). The systematically higher Ti concentration values for magnetite and pyrrhotite most likely reflect an increased spectral overlap between the Ti-K$_\alpha$ fluorescent peak and the more prominent Fe-K$_\alpha$ escape peak and, thus, should be considered with caution. The systematically lower Mn concentration values for magnetite, matrix and pyrrhotite most likely come from the over-estimation of the intensity of the low-energy tail of Fe during spectra fitting and, thus, should also be considered with caution. The concentration values of Ti and Mn are presented

nonetheless to show the influence of fitting errors which cannot be reduced by increasing the total number of MC simulations.

To better understand the influence of the accuracy of the main-element concentration values provided by the SEM–EDX setup on the calculated trace-element values, matrix #6 was simulated once more with the added step of applying a 25% Gaussian error (3 sigma) to all main elements used. For all calculated trace elements, there is an overlap of the 1 sigma error bar signifying that if the main elements used were varied by a few weight percent, the influence on the sample absorption correction factor and the final calculated trace elements is very minor. A plot with the trace-element concentration values of matrix #6, with and without main-element randomization, is presented as Additional file 3.

The CI normalized (Lodders, 2010) concentration values and standard deviations of trace elements in dolomite #4, apatite #7 and breunnerite #12 are shown in Fig. 9b. It is noticeable that, unlike for pyrrhotite
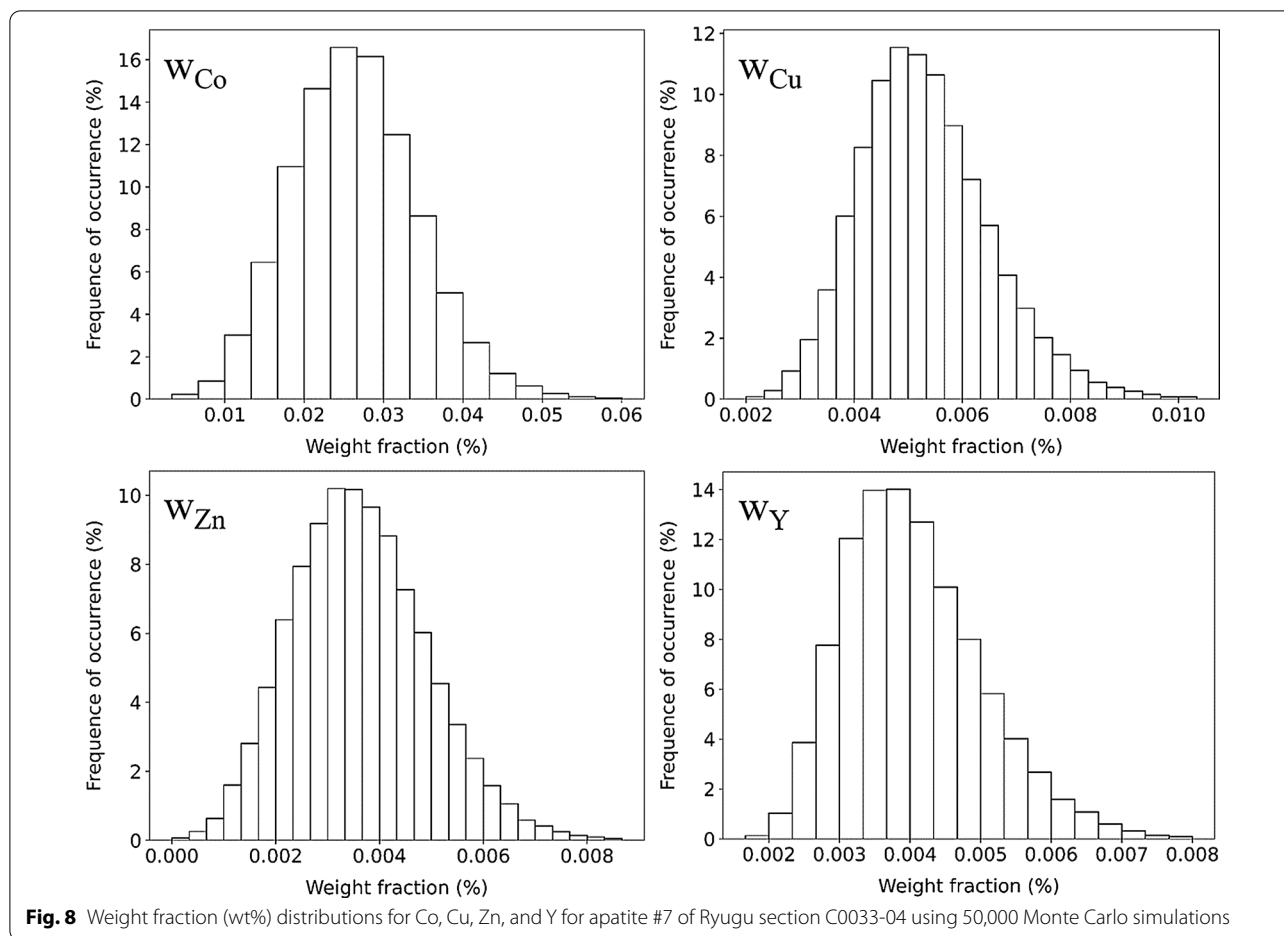
Bazi *et al. Earth, Planets and Space*   (2022) 74:161

Page 12 of 17

Table 3 Concentrations with standard deviations obtained for dolomite (dol), apatite (ap) and breunnerite (brn)

	#4	#9	#10	#13	#7	#8	#12
	Dolomite	Dolomite	Dolomite	Dolomite	Apatite	Apatite	Breunnerite
ρ(g/cm³)	2.86	2.86	2.86	2.86	3.1–3.15	3.1–3.15	3–3.1
T^{grain}(μm)	20–23	24–27	6–9	16–21	7–9	4–6	7–10
C	13.69**	13.69**	13.69**	13.69**	nd	nd	15.8**
F	nd	nd	nd	nd	1.74**	1.74**	nd
Na	nd	nd	nd	nd	0.93**	0.93**	nd
Mg	9.76**	9.76**	9.76**	9.76**	1.79**	1.79**	13.43**
Si	nd	nd	nd	nd	1.35**	1.35**	nd
P	nd	nd	nd	nd	16.32**	16.32**	nd
S	nd	nd	nd	nd	0.79**	0.79**	nd
Ca	17.66**	17.66**	17.66**	17.66**	34.42**	34.42**	0.71**
Ti	533±150	165±43	nd	353±223	nd	nd	nd
V	112±36	81±22	66±51	154±65	nd	nd	nd
Cr	0.23*±0.03*	542±64	nd	0.33*±0.07*	nd	0.15*±0.04*	nd
Mn	4.91**	4.91**	4.91**	4.91**	0.73**	0.73**	1.2**
Fe	2.03**	2.03**	2.03**	2.03**	2.11**	2.11**	13.44**
Co	368±57	115±21	46±35	229±44	264±80	nd	80±49
Ni	0.44*±0.07*	0.08*±0.01*	nd	0.21*±0.04*	0.34*±0.07*	nd	nd
Cu	27±6	7±2	28±11	6±3	53±12	nd	nd
Zn	93±17	15±3	69±27	37±8	36±13	nd	35±19
Ga	4±1	3±1	nd	5±1	nd	nd	3±1
Ge	8±2	3±1	5±3	5±2	nd	nd	4±2
As	nd	nd	5±2	nd	4±1	nd	5±2
Se	nd	nd	7±3	nd	11±3	nd	14±4
Sr	55±10	48±8	35±7	37±7	347±38	209±38	nd
Y	nd	nd	nd	nd	41±10	42±11	nd
Others	51.16*±0.11*	51.77*±0.02*	52.15*±1.31*	51.34*±0.12*	39.40*±0.08*	39.64*±0.35*	55.41*±0.01*

Data in ppm, except for the asterisk (*) representing data in wt%, the double asterisk (⁑) representing SEM–EDX data in wt% and the dagger (†) representing CI chondrite composition data from Lodders, 2010 in wt%. nd = not detected

and magnetite, the Ti values in the dolomite (#4) are not systematically higher, likely due to the absence of a prominent Fe-K$_\alpha$ escape peak. The Sr fluorescence peak is very high in the apatite grain (#7), less high in the dolomite grain (#4) and absent in the breunnerite grain (#12), which is in agreement with recent studies that show a strong correlation between Sr and Ca (Tkalcec et al. 2022) in carbonaceous chondrite material. Y is recorded only in the apatite grain (#7), where it shows a high and strong peak and is absent in all other mineral grains. Our trace element quantification results of the two polished sections C0033-01 and C0033-04 support the proposition that Ryugu samples, its bulk matrix composition and the mineral grains present, are CI-like. The latter is in agreement with recent conclusions from first studies of Ryugu material inferred from the absence of submillimeter CAIs and chondrules in Ryugu material (Yada et al., 2022), the bulk elemental and isotopic analysis of A0106, A0107, C0107 and C0108 (Yokoyama et al., 2022), the bulk muonic X-ray spectroscopic analysis of 10 Ryugu coarse grains, i.e., C0002, A0026, A0064, A0067, A0094, C0025, C0033, C0061, C0076 and C0103 (Nakamura et al., 2022), the powder XRD patterns of a mixture of A0029, A0037 and C0087 and bulk INAA results of A0098 and C0068 (Ito et al., 2022).

Fig. 8 Weight fraction (wt%) distributions for Co, Cu, Zn, and Y for apatite #7 of Ryugu section C0033-04 using 50,000 Monte Carlo simulations

Conclusions

A PyMca-based approach, based on the work of Schoonjans et al. (2012), was developed to quantify confocal XRF data during synchrotron experiments having the potential to obtain real-time quantitative elemental information, which is of the essence during the initial analysis of unique space material. We have illustrated the effectiveness of this confocal quantification method by applying it on confocal sub-micron SR-XRF data collected at the PETRA III P06 beamline from sections of a unique extraterrestrial material: a pristine asteroidal mm-sized grain, C0033, returned by the JAXA's Hayabusa2 mission. It is shown that the bulk matrix of Ryugu grain C0033 is similar to CI chondrite element abundance and that the analyzed mineral grains roughly follow the pattern observed in similar CI material, as was also concluded by other bulk and/or destructive spectroscopic analysis methods, i.e., powder XRD, INAA and muonic XRF. Confocal SR-XRF with sub-micron resolution has proven to be a successful non-destructive and mineral grain specific analysis tool for the trace-element quantification of unique and precious material returned by the Hayabusa2 space mission. In this respect, it would be a valuable tool for near future sample return missions like the OSIRIS-REx's touch-and-go mission to B-type asteroid (101955) Bennu.
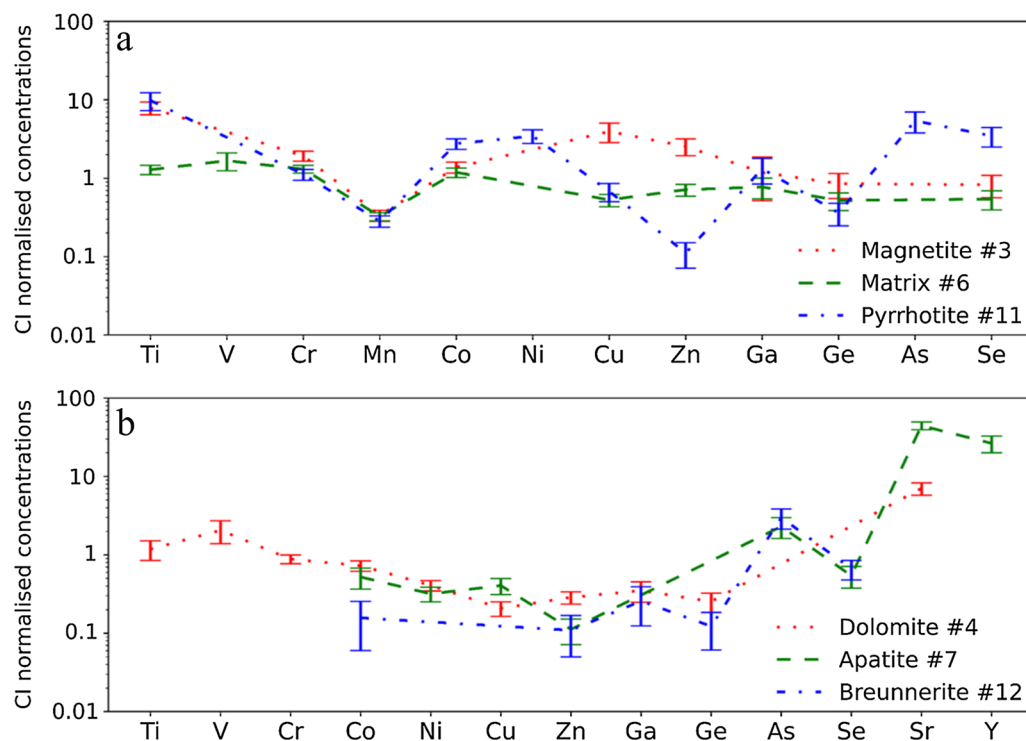
Fig. 9 a CI-normalised concentration values of trace elements in magnetite #3, matrix #6 and pyrrhotite #11. **b** CI-normalised concentration values of trace elements in dolomite #4, apatite #7 and breunnerite #12. CI normalisation is performed with CI chondrite composition data from Lodders, 2010. Error bars are 1 σ

Abbreviations
BSE: Backscatter electron; CT: Computed tomography; DESY: Deutches Elektronen-Synchrotron; DL: Detection limit; EDX: Energy-dispersive X-ray; INAA: Instrumental neutron activation analysis; JAXA: Japan Aerospace Exploration Agency; KB: Kirkpatrick-Baez; MC: Monte Carlo; SDD: Silicon drift detector; SEM: Secondary electron microscopy; SCI: Small carry-on impactor; SR: Synchrotron radiation; TD2: Touchdown 2; XOS: X-ray optics and sources; XRD: X-ray diffraction; XRF: X-ray fluorescence.

Supplementary Information
The online version contains supplementary material available at https://doi.org/10.1186/s40623-022-01726-y.

> **Additional file 1:** Monte Carlo uncertainty estimation method for the calculation of the elemental yields.
>
> **Additional file 2:** Monte Carlo uncertainty estimation method for the calculation of the mineral grain weight fractions.
>
> **Additional file 3:** Trace-element concentration values of matrix #6, with and without main-element randomization.

Author contributions
BB contributed to the SR-XRF measurements, was leading the confocal data processing and was the main author of this manuscript. ML contributed to the SR-XRF measurements, analyzed the CT data and did SEM–EDX measurements. PT, BV and LV contributed to the SR-XRF measurements and the confocal data processing. BJT and FEB were involved in the SEM–EDX measurements and data processing. They also contributed to the SR-XRF measurements, the confocal data evaluation and cosmochemical interpretation. JG and GF helped with the SR-XRF measurements as beamline scientists of beamline P06 at PETRA III. TN provided the Ryugu samples, SR-CT data and BSE images. All authors read and approved the final manuscript.

Availability of data and materials
Data are available from the authors upon reasonable request.

Declarations

Ethics approval and consent to participate
Not applicable

Consent for publication
Not applicable

Competing interests
No competing interest is declared.

Author details
[1]Department of Chemistry, Ghent University, Krijgslaan 281 S12, B-9000 Ghent, Belgium. [2]Department of Geosciences, Goethe University Frankfurt,

Bazi *et al. Earth, Planets and Space*   (2022) 74:161

Page 15 of 17

Altenhoeferallee 1, 60438 Frankfurt am Main, Germany. [3]Deutsches Elektronen-Synchrotron, DESY, Notkestraße 85, 22607 Hamburg, Germany. [4]Graduate School of Advanced Science and Engineering, Hiroshima University, Higashi-Hiroshima 739-8526, Japan. [5]Department of Natural History Sciences, Hokkaido University, Sapporo 060-0810, Japan. [6]Department of Earth Science, Tohoku University, Aoba-Ku, Sendai 980-8578, Japan. [7]JASRI/SPring-8, Sayo 679-5198, Japan. [8]Department of Earth and Planetary Sciences, Kyushu University, Fukuoka 812-8581, Japan. [9]Laboratory for Planetary Sciences, Kyoto University, Kyoto 606-8502, Japan. [10]Institute of Space and Astronautical Science (ISAS), Japan Aerospace Exploration Agency (JAXA), Sagamihara 252-5210, Japan. [11]Kanagawa Institute of Technology, Atsugi 243-0292, Japan. [12]Department of Earth and Planetary Science, The University of Tokyo, Tokyo 113-0033, Japan. [13]Department of Earth and Planetary Sciences, Nagoya University, Furo-Cho Chikusa-Ku, Nagoya 464-8601, Japan.

References

Arakawa M, Saiki T, Wada K, Ogawa K, Kadono T, Shirai K, Sawada H, Ishibashi K, Honda R, Sakatani N, Iijima Y, Okamoto C, Yano H, Takagi Y, Hayakawa M, Michel P, Jutzi M, Shimaki Y, Kimura S, Mimasu Y, Toda T, Imamura H, Nakazawa S, Hayakawa H, Sugita S, Morota T, Kameda S, Tatsumi E, Cho Y, Yoshioka K, Yokota Y, Matsuoka M, Yamada M, Kouyama T, Honda C, Tsuda Y, Watanabe S, Yoshikawa M, Tanaka S, Terui F, Kikuchi S, Yamaguchi T, Ogawa N, Ono G, Yoshikawa K, Takahashi T, Takei Y, Fujii A, Takeuchi H, Yamamoto Y, Okada T, Hirose C, Hosoda S, Mori O, Shimada T, Soldini S, Tsukizaki R, Iwata T, Ozaki M, Abe M, Namiki N, Kitazato K, Tachibana S, Ikeda H, Hirata N, Hirata N, Noguchi R, Miura A (2020) An artificial impact on the asteroid (162173) Ryugu formed a crater in the gravity-dominated regime. Science 368(6486):67–71

Beckhoff B, Kanngießer B, Langhoff N, Wedell R, Wolff H (eds) (2007) Handbook of practical X-ray fluorescence analysis. Springer Science & Business Media, Berlin

Borisova AY, Freydier R, Polvé M, Jochum KP, Candaudap F (2010) Multi-elemental analysis of ATHO-G rhyolitic glass (MPI-DING reference material) by femtosecond and nanosecond LA-ICP-MS: evidence for significant heterogeneity of B, V, Zn, Mo, Sn, Sb, Cs, W, Pt and Pb at the millimetre scale. Geostand Geoanal Res 34(3):245–255

Bowles JFW, Howie RA, Vaughan DJ, Zussman J (2011) Rock-forming minerals. Volume 5A non-silicates: oxides, hydroxides and sulphides, 2nd edn. The Geological Society, London, pp 237–239

Brenker FE, Westphal AJ, Vincze L, Burghammer M, Schmitz S, Schoonjans T, Silversmit G, Vekemans B, Allen C, Anderson D, Ansari A, Bajt S, Bastien RK, Bassim N, Bechtel HA, Borg J, Bridges J, Brownlee DE, Burchell M, Butterworth AL, Changela H, Cloetens P, Davis AM, Doll R, Floss C, Flynn G, Fougeray P, Frank DR, Gainsforth Z, Grün E, Heck PR, Hillier JK, Hoppe P, Hudson B, Huth J, Hvide B, Kearsley A, King AJ, Lai B, Leitner J, Lemelle L, Leroux H, Leonard A, Lettieri R, Marchant W, Nittler LR, Ogliore R, Ong WJ, Postberg F, Price MC, Sandford SA, Tresseras J-AS, Simionovici AS, Solé VA, Srama R, Stadermann F, Stephan T, Sterken VJ, Stodolna J, Stroud RM, Sutton S, Trieloff M, Tsou P, Tsuchiyama A, Tyliszczak T, Korff JV, Wordsworth N, Zevin D, Zolensky ME, >30,000 Stardust@home (2014) Stardust Interstellar Preliminary Examination V: XRF analyses of interstellar dust candidates at ESRF ID 13. Meteor Planet Sci 49(9):1594–1611

Chang LLY, Howie RA, Zussman J (1996) Rock-forming minerals, vol 5B: Non Silicates. Longman, Harlow, Essex, pp 108–135

Flynn GJ (2007) Physical, chemical, and mineralogical properties of comet 81P/Wild 2 particles collected by Stardust. Advances in Meteoroid and Meteor Science. Springer, New York, pp 447–459

Flynn GJ, Bleuet P, Borg J, Bradley J, Brenker FE, Brennan S, Bridges J, Brownlee DE, Bullock E, Clark BC, Dai ZR, Daghlian C, Djouadi Z, Fakra S, Ferroir T, Floss C, Franchi IA, Gainsforth Z, Gallien J-P, Gillet P, Grant PG, Graham GA, Green SF, Grossemy F, Heck P, Herzog GF, Hoppe P, Hörz F, Huth J, Ignatyev KI, Ishii HA, Joswiak D, Kearsley AT, Khodja H, Lanzirotti A, Leitner J, Lemelle L, Leroux H, Luening K, MacPherson G, Marhas KK, Marcus MA, Matrajt G, Nakamura T, Nakano T, Newville M, Papanastassiou DA, Pianetta P, Rao W, Rietmeijer FJM, Rost D, Schwandt CS, See TH, Sheffield-Parker J, Simionovici A, Sitnitsky I, Snead CJ, Stadermann FJ, Stephan T, Stroud

RM, Susini J, Suzuki Y, Sutton SR, Taylor S, Teslich N, Troadec D, Tsou P, Tsuchiyama A, Uesugi K, Westphal A, Wozniakiewicz P, Vicenzi E, Vincze L, Zolensky ME (2006) Elemental compositions of comet 81P/Wild 2 samples collected by Stardust. Science 314(5806):1731–1735

Gounelle M, Zolensky ME (2001) A terrestrial origin for sulfate veins in CI1 chondrites. Meteorit Planet Sci 36(10):1321–1329

Greshake A, Klock W, Arndt P, Maetz M, Bischoff A (1994) Pulse heating of fragments from Orgueil (CI): simulation of atmospheric entry heating of micrometeorites. Meteoritics 29:470

Greshake A, Flynn GJ, Bajt S (1997) Trace element concentrations in pyrrhotites from Orgueil (CI). Lunar Planet Sci Conf 28:465

Ito M, Takano Y, Kebukawa Y, Ohigashi T, Matsuoka M, Kiryu K, Uesugi M, Nakamura T, Yuzawa H, Yamada K, Naraoka H, Yada T, Abe M, Hayakawa M, Saiki T, Tachibana S, Hayabusa2 Project Team (2021) Assessing the debris generated by the small carry-on impactor operated from the Hayabusa2 mission. Geochem J 55(4):223–239

Lauretta DS, DellaGiustina DN, Bennett CA, Golish DR, Becker KJ, Balram-Knutson SS, Barnouin OS, Becker TL, Bottke WF, Boynton WV, Campins H, Clark BE, Connolly HC Jr, Drouet d'Aubigny CY, Dworkin JP, Emery JP, Enos HL, Hamilton VE, Hergenrother CW, Howell ES, Izawa MRM, Kaplan HH, Nolan MC, Rizk B, Roper HL, Scheeres DJ, Smith PH, Walsh KJ, Wolner CWV (2019) The unexpected surface of asteroid (101955) Bennu. Nature 568(7750):55–60

Limaye A (2012) Drishti: a volume exploration and presentation tool. Developments in X-ray Tomography VIII, 8506, p.85060X

Lodders K (2010) Solar system abundances of the elements. Principles and perspectives in cosmochemistry. 379–417.

Nakamura T, Matsumoto M, Amano K, Enokido Y, Zolensky ME, Mikouchi T, Genda H, Tanaka S, Zolotov MY, Kurosawa K, Wakita S, Hyodo R, Nagano H, Nakashima D, Takahashi Y, Fujioka Y, Kikuiri M, Kagawa E, Matsuoka M, Brearley AJ, Tsuchiyama A, Uesugi M, Matsuno J, Kimura Y, Sato M, Milliken RE, Tatsumi E, Sugita S, Hiroi T, Kitazato K, Brownlee D, Joswiak DJ, Takahashi M, Ninomiya K, Takahashi T, Osawa T, Terada K, Brenker FE, Tkalcec BJ, Vincze L, Brunetto R, Aléon-Toppani A, Chan QHS, Roskosz M, Viennet J-C, Beck P, Alp EE, Michikami T, Nagaashi Y, Tsuji T, Ino Y, Martinez J, Han J, Dolocan A, Bodnar RJ, Tanaka M, Yoshida H, Sugiyama K, King AJ, Fukushi K, Suga H, Yamashita S, Kawai T, Inoue K, Nakato A, Noguchi T, Vilas F, Hendrix AR, Jaramillo C, Domingue DL, Dominguez G, Gainsforth Z, Engrand C, Duprat J, Russell SS, Bonato E, Ma C, Kawamoto T, Wada T, Watanabe S, Endo R, Enju S, Riu L, Rubino S, Tack P, Takeshita S, Takeichi Y, Takeuchi A, Takigawa A, Takir D, Tanigaki T, Taniguchi A, Tsukamoto K, Yagi T, Yamada S, Yamamoto K, Yamashita Y, Yasutake M, Uesugi K, Umegaki I, Chiu I, Ishizaki T, Okumura S, Palomba E, Pilorget C, Potin SM, Alasli A, Anada S, Araki Y, Sakatani N, Schultz C, Sekizawa O, Sitzman SD, Sugiura K, Sun M, Dartois E, De Pauw E, Dionnet Z, Djouadi Z, Falkenberg G, Fujita R, Fukuma T, Gearba IR, Hagiya K, Hu MY, Kato T, Kawamura T, Kimura M, Kubo MK, Langenhorst F, Lantz C, Lavina B, Lindner M, Zhao J, Vekemans B, Baklouti D, Bazi B, Borondics F, Nagasawa S, Nishiyama G, Nitta K, Mathurin J, Matsumoto T, Mitsukawa I, Miura H, Miyake A, Miyake Y, Yurimoto H, Okazaki R, Yabuta H, Naraoka H, Sakamoto K, Tachibana S, Connolly HC Jr, Lauretta DS, Yoshitake M, Yoshikawa M, Yoshikawa K, Yoshihara K, Yokota Y, Yogata K, Yano H, Yamamoto Y, Yamamoto D, Yamada M, Yamada T, Yada T, Wada K, Usui T, Tsukizaki R, Terui F, Takeuchi H, Takei Y, Iwamae A, Soejima H, Shirai K, Shimaki Y, Senshu H, Sawada H, Saiki T, Ozaki M, Ono G, Okada T, Ogawa N, Ogawa K, Noguchi R, Noda H, Nishimura M, Namiki N, Nakazawa S, Morota T, Miyazaki A, Miura A, Mimasu Y, Matsumoto K, Kumagai K, Kouyama T, Kikuchi S, Kawahara K, Kameda S, Iwata T, Ishihara Y, Ishiguro M, Ikeda H, Hosoda S, Honda R, Honda C, Hitomi Y, Hirata N, Hirata N, Hayashi T, Hayakawa M, Hatakeda K, Furuya S, Fukai R, Fujii A, Cho Y, Arakawa M, Abe M, Watanabe S, Tsuda Y (2022) Formation and evolution of carbonaceous asteroid Ryugu: direct evidence from returned samples. Science. https://doi.org/10.1126/science.abn8671

Newbury DE, Ritchie NW (2013) Is scanning electron microscopy/energy dispersive X-ray spectrometry (SEM/EDS) quantitative? Scanning 35(3):141–168

Newbury DE, Swyt CR, Myklebust RL (1995) "Standardless" quantitative electron probe microanalysis with energy-dispersive X-ray spectrometry: is it worth the risk? Anal Chem 67(11):1866–1871

O'Neill ME (2014) PCG: a family of simple fast space-efficient statistically good algorithms for random number generation. ACM Trans Math Softw

Bazi *et al. Earth, Planets and Space*   (2022) 74:161

Page 16 of 17

Rudraswami NG, Prasad MS, Dey S, Plane JMC, Feng W, Taylor S (2015) Evaluating changes in the elemental composition of micrometeorites during entry into the Earth's atmosphere. Astrophys J 814(1):78

Saiki T, Imamura H, Arakawa M, Wada K, Takagi Y, Hayakawa M, Shirai K, Yano H, Okamoto C (2017) The small carry-on impactor (SCI) and the Hayabusa2 impact experiment. Space Sci Rev 208(1):165–186

Saiki T, Takei Y, Takahashi T, Kikuchi S, Sawada H, Hirose C, Terui F, Ogawa N, Mimasu Y, Ono G, Yoshikawa K, Takeushi H, Fujii A, Masuda T, Yasuda S, Matsushima K, Yoshikawa M, Nakazawa S, Tsuda Y, Hayabusa2 Project Team (2021) Overview of Hayabusa2 asteroid proximity operation planning and preliminary results. Trans Jpn Soc Aeronaut Space Sci Aerosp Technol Jpn 19(1):52–60

Schmitz S, Brenker FE, Schoonjans T, Vekemans B, Silversmit G, Vincze L, Burghammer M, Riekel C (2009) In-situ identification of CAI candidate in Wild 2 cometary dust by high resolution SR-XRF. Geochim Cosmochim Acta 73:5483–5492

Schoonjans T, Brunetti A, Golosio B, del Rio MS, Solé VA, Ferrero C, Vincze L (2011a) The xraylib library for x-ray-matter interaction cross sections: new developments and applications. Adv Comput Methods X-Ray Opt II 8141:8141110

Schoonjans T, Brunetti A, Golosio B, del Rio MS, Solé VA, Ferrero C, Vincze L (2011b) The xraylib library for X-ray–matter interactions. Recent developments. Spectrochimica Acta Part B at Spectrosc 66(11–12):776–784

Schoonjans T, Silversmit G, Vekemans B, Schmitz S, Burghammer M, Riekel C, Brenker FE, Vincze L (2012) Fundamental parameter based quantification algorithm for confocal nano-X-ray fluorescence analysis. Spectrochim Acta Part B 67:32–42

Schroer CG, Boye P, Feldkamp JM, Patommel J, Samberg D, Schropp A, Schwab A, Stephan S, Falkenberg G, Wellenreuther G, Reimers N (2010) Hard X-ray nanoprobe at beamline P06 at PETRA III. Nucl Instrum Methods Phys Res Sect A 616(2–3):93–97

Silversmit G, Vekemans B, Brenker FE, Schmitz S, Burghammer M, Riekel C, Vincze L (2009) X-ray Fluorescence Nanotomography on Cometary Matter from Comet 81P/Wild2 Returned by Stardust. Anal Chem 81:6107–6112

Singerling SA, Sutton SR, Lanzirotti A, Newville M, Brearley AJ (2021) Trace elemental behavior in the solar nebula: synchrotron X-ray fluorescence analyses of CM and CR chondritic iron sulfides and associated metal. Geochim Cosmochim Acta 310:131–154

Solé VA, Papillon E, Cotte M, Walter P, Susini JA (2007) A multiplatform code for the analysis of energy-dispersive X-ray fluorescence spectra. Spectrochim Acta Part B 62(1):63–68

Sugita S, Honda R, Morota T, Kameda S, Sawada H, Tatsumi E, Yamada M, Honda C, Yokota Y, Kouyama T, Sakatani N, Ogawa K, Suzuki H, Okada T, Namiki N, Tanaka S, Iijima Y, Yoshioka K, Hayakawa M, Cho Y, Matsuoka M, Hirata N, Hirata N, Miyamoto H, Domingue D, Hirabayashi M, Nakamura T, Hiroi T, Michikami T, Michel P, Ballouz R-L, Barnouin OS, Ernst CM, Schröder SE, Kikuchi H, Hemmi R, Komatsu G, Fukuhara T, Taguchi M, Arai T, Senshu H, Demura H, Ogawa Y, Shimaki Y, Sekiguchi T, Müller TG, Hagermann A, Mizuno T, Noda H, Matsumoto K, Yamada R, Ishihara Y, Ikeda H, Araki H, Yamamoto K, Abe S, Yoshida F, Higuchi A, Sasaki S, Oshigami S, Tsuruta S, Asari K, Tazawa S, Shizugami M, Kimura J, Otsubo T, Yabuta H, Hasegawa S, Ishiguro M, Tachibana S, Palmer E, Gaskell R, Le Corre L, Jaumann R, Otto K, Schmitz N, Abell PA, Barucci MA, Zolensky ME, Vilas F, Thuillet F, Sugimoto C, Takaki N, Suzuki Y, Kamiyoshihara H, Okada M, Nagata K, Fujimoto M, Yoshikawa M, Yamamoto Y, Shirai K, Noguchi R, Ogawa N, Terui F, Kikuchi S, Yamaguchi T, Oki Y, Takao Y, Takeuchi H, Ono G, Mimasu Y, Yoshikawa K, Takahashi T, Takei Y, Fujii A, Hirose C, Nakazawa S, Hosoda S, Mori O, Shimada T, Soldini S, Iwata T, Abe M, Yano H, Tsukizaki R, Ozaki M, Nishimura K, Saiki T, Watanabe S, Tsuda Y (2019) The geomorphology, color, and thermal properties of Ryugu: implications for parent-body processes. Science 364(6437):eaaw422

Tachibana S (2021) The Hayabusa2 mission what will we expect from samples from C-type near-Earth asteroid (162173) Ryugu? Sample Return Missions. Elsevier, Amsterdam, pp 147–162

Tachibana S, Sawada H, Okazaki R, Takano Y, Sakamoto K, Miura YN, Okamoto C, Yano H, Yamanouchi S, Michel P, Zhang Y, Schwartz S, Thuillet F, Yurimoto H, Nakamura T, Noguchi T, Yabuta H, Naraoka H, Tsuchiyama A, Imae N, Kurosawa K, Nakamura AM, Ogawa K, Sugita S, Morota T, Honda R, Kameda S, Tatsumi E, Cho Y, Yoshioka K, Yokota Y, Hayakawa M, Matsuoka M, Sakatani N, Yamada M, Kouyama T, Suzuki H, Honda C,

Yoshimitsu T, Kubota T, Demura H, Yada T, Nishimura M, Yogata K, Nakato A, Yoshitake M, Suzuki AI, Furuya S, Hatakeda K, Miyazaki A, Kumagai K, Okada T, Abe M, Usui T, Ireland TR, Fujimoto M, Yamada T, Arakawa M, Connolly HC Jr, Fujii A, Hasegawa S, Hirata N, Hirata N, Hirose C, Hosoda S, Iijima Y, Ikeda H, Ishiguro M, Ishihara Y, Iwata T, Kikuchi S, Kitazato K, Lauretta DS, Libourel G, Marty B, Matsumoto K, Michikami T, Mimasu Y, Miura A, Mori O, Nakamura-Messenger K, Namiki N, Nguyen AN, Nittler LR, Noda H, Noguchi R, Ogawa N, Ono G, Ozaki M, Senshu H, Shimada T, Shimaki Y, Shirai K, Soldini S, Takahashi T, Takei Y, Takeuchi H, Tsukizaki R, Wada K, Yamamoto Y, Yoshikawa K, Yumoto K, Zolensky ME, Nakazawa S, Terui F, Tanaka S, Saiki T, Yoshikawa M, Watanabe S, Tsuda Y (2022) Pebbles and sand on asteroid (162173) Ryugu: In situ observation and particles returned to Earth. Science 375(6584):1011–1016

Tkalcec BJ, Tack P, De Pauw E, Vekemans B, Nakamura T, Garrevoet J, Falkenberg G, Vincze L, Brenker FE (2022) Sr distribution as proxy for Ca distribution at depth in SXRF analysis of mm-sized carbonaceous chondrites: implications for asteroid sample return missions. Meteorit Planet Sci 57:1–13

Vincze L, Vekemans B, Brenker FE, Falkenberg G, Rickers K, Somogyi A, Kersten M, Adams F (2004) Three-dimensional trace element analysis by confocal X-ray microfluorescence imaging. Anal Chem 76(22):6786–6791

Watanabe S, Hirabayashi M, Hirata N, Hirata N, Noguchi R, Shimaki Y, Ikeda H, Tatsumi E, Yoshikawa M, Kikuchi S, Yabuta H, Nakamura T, Tachibana S, Ishihara Y, Morota T, Kitazato K, Sakatani N, Matsumoto K, Wada K, Senshu H, Honda C, Michikami T, Takeuchi H, Kouyama T, Honda R, Kameda S, Fuse T, Miyamoto H, Komatsu G, Sugita S, Okada T, Namiki N, Arakawa M, Ishiguro M, Abe M, Gaskell R, Palmer E, Barnouin OS, Michel P, French AS, McMahon JW, Scheeres DJ, Abell PA, Yamamoto Y, Tanaka S, Shirai K, Matsuoka M, Yamada M, Yokota Y, Suzuki H, Yoshioka K, Cho Y, Tanaka S, Nishikawa N, Sugiyama T, Kikuchi H, Hemmi R, Yamaguchi T, Ogawa N, Ono G, Mimasu Y, Yoshikawa K, Takahashi T, Takei Y, Fujii A, Hirose C, Iwata T, Hayakawa M, Hosoda S, Mori O, Sawada H, Shimada T, Soldini S, Yano H, Tsukizaki R, Ozaki M, Iijima Y, Krause C, Terui F, Saiki T, Nakazawa S, Tsuda Y (2019) Hayabusa2 arrives at the carbonaceous asteroid 162173 Ryugu—a spinning top–shaped rubble pile. Science 364(6437):268–272

Westphal AJ, Stroud RM, Bechtel HA, Brenker FE, Butterworth AL, Flynn GJ, Frank DR, Gainsforth Z, Hillier JK, Postberg F, Simionovici AS, Sterken VJ, Nittler LR, Allen C, Anderson D, Ansari A, Bajt S, Bastien RK, Bassim N, Bridges J, Brownlee DE, Burchell M, Burghammer M, Changela H, Cloetens P, Davis AM, Doll R, Floss C, Grün E, Heck PR, Hoppe P, Hudson B, Huth J, Kearsley A, King AJ, Lai B, Leitner J, Lemelle L, Leonard A, Leroux H, Lettieri R, Marchant W, Ogliore R, Ong WJ, Price MC, Sandford SA, Tresseras J-AS, Schmitz S, Schoonjans T, Schreiber K, Silversmit G, Solé VA, Srama R, Stadermann F, Stephan T, Stodolna J, Sutton S, Trieloff M, Tsou P, Tyliszczak T, Vekemans B, Vincze L, Von Korff J, Wordsworth N, Zevin D, Zolensky ME, 30714 Stardust@home dusters (2014) Evidence for interstellar origin of seven dust particles collected by the Stardust spacecraft. Science 345(6198):786–791

Yada T, Abe M, Okada T, Nakato A, Yogata K, Miyazaki A, Hatakeda K, Kumagai K, Nishimura M, Hitomi Y, Soejima H, Yoshitake M, Iwamae A, Furuya S, Uesugi M, Karouji Y, Usui T, Hayashi T, Yamamoto D, Fukai R, Sugita S, Cho Y, Yumoto K, Yabe Y, Bibring J-P, Pilorget C, Hamm V, Brunetto R, Riu L, Lourit L, Loizeau D, Lequertier G, Moussi-Soffys A, Tachibana S, Sawada H, Okazaki R, Takano Y, Sakamoto K, Miura YN, Yano H, Ireland TR, Yamada T, Fujimoto M, Kitazato K, Namiki N, Arakawa M, Hirata N, Yurimoto H, Nakamura T, Noguchi T, Yabuta H, Naraoka H, Ito M, Nakamura E, Uesugi K, Kobayashi K, Michikami T, Kikuchi H, Hirata N, Ishihara Y, Matsumoto K, Noda H, Noguchi R, Shimaki Y, Shirai K, Ogawa K, Wada K, Senshu H, Yamamoto Y, Morota T, Honda R, Honda C, Yokota Y, Matsuoka M, Sakatani N, Tatsumi E, Miura A, Yamada M, Fujii A, Hirose C, Hosoda S, Ikeda H, Iwata T, Kikuchi S, Mimasu Y, Mori O, Ogawa N, Ono G, Shimada T, Soldini S, Takahashi T, Takei Y, Takeuchi H, Tsukizaki R, Yoshikawa K, Terui F, Nakazawa S, Tanaka S, Saiki T, Yoshikawa M, Watanabe S, Tsuda Y (2022) Preliminary analysis of the Hayabusa2 samples returned from C-type asteroid Ryugu. Nature Astronomy 6(2):214–220

Yokoyama T, Nagashima K, Nakai I, Young ED, Abe Y, Aléon J, Alexander CMO'D, Amari S, Amelin Y, Bajo K-I, Bizzarro M, Bouvier A, Carlson RW, Chaussidon M, Choi B-G, Dauphas N, Davis AM, Di Rocco T, Fujiya W, Fukai R, Gautam I, Haba MK, Hibiya Y, Hidaka H, Homma H, Hoppe P, Huss GR, Ichida K, Iizuka T, Ireland TR, Ishikawa A, Ito M, Itoh S, Kawasaki N, Kita NT, Kitajima O, Kleine T, Komatani S, Krot AN, Liu M-C, Masuda Y, McKeegan KD, Morita

Bazi *et al. Earth, Planets and Space*   (2022) 74:161

Page 17 of 17

M, Motomura K, Moynier F, Nguyen A, Nittler L, Onose M, Pack A, Park C, Piani L, Qin L, Russell SS, Sakamoto N, Schönbächler M, Tafla L, Tang H, Terada K, Terada Y, Usui T, Wada S, Wadhwa M, Walker RJ, Yamashita K, Yin Q-Z, Yoneda S, Yui H, Zhang A-C, Connolly HC Jr, Lauretta DS, Nakamura T, Naraoka H, Noguchi T, Okazaki R, Sakamoto K, Yabuta H, Abe M, Arakawa M, Fujii A, Hayakawa M, Hirata N, Hirata N, Honda R, Honda C, Hosoda S, Iijima Y, Ikeda H, Ishiguro M, Ishihara Y, Iwata T, Kawahara K, Kikuchi S, Kitazato K, Matsumoto K, Matsuoka M, Michikami T, Mimasu Y, Miura A, Morota T, Nakazawa S, Namiki N, Noda H, Noguchi R, Ogawa N, Ogawa K, Okada T, Okamoto C, Ono G, Ozaki M, Saiki T, Sakatani N, Sawada H, Senshu H, Shimaki Y, Shirai K, Sugita S, Takei Y, Takeuchi H, Tanaka S, Tatsumi E, Terui F, Tsuda Y, Tsukizaki R, Wada K, Watanabe S, Yamada M, Yamada T, Yamamoto Y, Yano H, Yokota Y, Yoshihara K, Yoshikawa M, Yoshikawa K, Furuya S, Hatakeda K, Hayashi T, Hitomi Y, Kumagai K, Miyazaki A, Nakato A, Nishimura M, Soejima H, Suzuki A, Yada T, Yamamoto D, Yogata K, Yoshitake M, Tachibana S, Yurimoto H (2022) Samples returned from the asteroid Ryugu are similar to Ivuna-type carbonaceous meteorites. Science. https://doi.org/10.1126/science.abn7850

Zolensky ME, Zega TJ, Yano H, Wirick S, Westphal AJ, Weisberg MK, Weber I, Warren JL, Velbel MA, Tsuchiyama A, Tsou P, Toppani A, Tomioka N, Tomeoka K, Teslich N, Taheri M, Susini J, Stroud R, Stephan T, Stadermann FJ, Snead CJ, Simon SB, Siminovici A, See TH, Robert F, Rietmeijer FJM, Rao W, Perronnet MC, Papanastassiou DA, Okudaira K, Ohsumi K, Ohnishi I, Nakanura-Messenger K, Nakamura T, Mostefaoui S, Mikouchi T, Meibom A, Matrajt G, Marcus MA, Leroux H, Lemelle L, Le L, Lanzirotti A, Langenhorst F, Krot AN, Keller LP, Kearsley AT, Joswiak D, Jacob D, Ishii H, Harvey R, Hagiya K, Grossman L, Graham GA, Gounelle M, Gillet P, Genge MJ, Flynn G, Ferrior T, Fallon S, Ebel DS, Dai ZR, Cordier P, Chi M, Butterworth AL, Brownlee DE, Bridges JC, Brennan S, Brearley A, Bradley JP, Bleuet P, Bland PA, Bastien R (2006) Mineralogy and petrology of comet 81P/Wild 2 nucleus samples. Science 314(5806):1735–1739

Publisher's Note

Springer Nature remains neutral with regard to jurisdictional claims in published maps and institutional affiliations.